

Efficient electrocatalytic overall water splitting of porous 3D CoPt₃/a-FCWO-NS heterostructures: Morphology modulation and interfacial engineering for the formation of crystalline-amorphous nanosheets

Zhenlong Wang^{a,b}, Sirong Li^a, Guofei Zhang^a, Xin Yu^a, Zhengyi Zhao^a, Yipeng Zhang^a, Yang Shi^a, Hai-Bin Zhu^{b,*}, Xuechun Xiao^{a,*}

^a School of Materials and Energy, Yunnan University, 650504 Kunming, People's Republic of China

^b School of Chemistry and Chemical Engineering, Southeast University, 211189 Nanjing, People's Republic of China



ARTICLE INFO

Keywords:

Water splitting
Morphology modulation
Interface engineering
Heterostructures
3D nanosheets

ABSTRACT

Achieving efficient oxygen evolution reaction (OER) and hydrogen evolution reaction (HER) simultaneously in the electrocatalytic water-splitting is essential to achieve a green hydrogen economy. However, a rational catalyst design still faces great challenges due to the slow kinetic limitations such as electron transfer at the electrode-electrolyte interface. Herein, a porous 3D CoPt₃/a-FCWO-NS heterostructures was formed by morphology modulation and interfacial engineering. Notably, the catalyst requires only 1.51 V to achieve 10 mA cm⁻² in 1 M KOH, and a commercial 1.5 V cell can drive the overall water-splitting with excellent stability. DFT combined with XPS results reveal the electron transfer between CoPt₃ and FeCoW oxides. Due to the ensemble effect CoPt₃ exhibits an electron deficient state moderating the slow kinetics of the OER process. Furthermore, the substrate FeCoW oxides modulates the d-band position of CoPt₃, and the suitable adsorption energy for hydrogen-containing intermediates makes CoPt₃/a-FCWO favorable for the HER process.

1. Introduction

Hydrogen energy is widely regarded as a promising alternative to conventional fossil fuels due to its sustainability, lack of carbon emissions, and ability to provide high-energy output as a secondary energy source [1]. Industrial hydrogen production processes, such as fossil energy hydrogen production, industrial by-product hydrogen production, electrolytic water hydrogen production, and renewable energy hydrogen production, have reached a state of maturity. However, except for electrolytic hydrogen production, the remaining three methods of industrial hydrogen production are characterized by inefficiency and pollution, either due to the low purity of hydrogen produced or the generation of CO₂. The electrocatalytic water splitting plant serves as a renewable energy conversion device that offers a viable solution to the environmental pollution issues arising from the depletion and combustion of fossil energy sources [2,3]. The issue of sluggish kinetics observed during the process of water electrolysis represents a significant obstacle in current research [4,5]. Considering this rationale, it is of utmost significance to expedite the reaction process through the

incorporation of highly effective catalysts onto the electrode surface. This will facilitate the rapid adsorption of intermediates and enhance the interaction with the electrode surfaces.

Noble metal-based catalysts have been extensively studied in the context of water splitting [6], urea decomposition [7], and metal-air cells [8–10]. This is attributed to their optimal d-orbital electron count and their capacity to adsorb and desorb intermediates during catalytic reactions [11,12]. Pt-based catalysts exhibit remarkable performance in the HER owing to their optimal interaction with the surface hydrogen adsorbent [13]. However, achieving superior performance in the OER remains challenging. Pt-based catalysts pose challenges for practical application due to their high cost and limited stability. In recent years, there has been a significant research focus on transition metal-based catalysts in the field of electrocatalysis. This is primarily due to their abundant reserves and high activity levels, making them a promising area of study [14–16]. Among the various catalytic materials, Fe-Co-based and Co-W-based catalysts [17,18] have demonstrated great potential for numerous applications in electrocatalytic water splitting. This is attributed to their favorable electronic band structure, high

* Corresponding authors.

E-mail addresses: zhuhabin@seu.edu.cn (H.-B. Zhu), xchxiao@ynu.edu.cn (X. Xiao).

electrical conductivity, and cost-effectiveness. Fe-Co-W-based catalytic materials have also been partially reported for OER [19–21], but their application in achieving high-performance, low-loss bifunctional electrocatalytic hydrolysis is less reported. Impressively, materials with amorphous structures are widely used in electrocatalysis due to their abundance of defects, structural flexibility, and other advantages [22–24]. However, it is limited in practical applications due to its poor electrical conductivity and stability. Although the crystal structure material has excellent good electrical conductivity as well as stability and suitable adsorption energy in the intermediate adsorption process, it still has the problem of a slow water dissociation process. Therefore, it becomes a possibility to use the strong coupling of constructing crystalline-amorphous heterostructures for improving the OER and HER performance of catalysts. Nevertheless, it is still a challenge to design catalysts with a low content of platinum to reduce the energy barrier in the HER process while maintaining the activity of the OER.

Till now, more reports are mainly on carbon-based loaded metal catalysts, such as single atoms, metal clusters and nanoparticles loaded on carbon nanotubes, graphene [25,26]. However, loading on metal oxides has been reported less frequently, and the simultaneous presence of amorphous-crystalline heterogeneous interfaces has been reported even less frequently. In this paper, we present a novel synthetic method which utilizes ultrasound-assisted reduction to enrich crystalline CoPt₃ alloys on the surface of amorphous FeCoW oxides. In addition, we successfully prepared ultrathin porous nano catalytic materials. These ultrathin nanosheets (CoPt₃/FCWO-NS) with crystalline amorphous heterostructures greatly facilitate the HER process in alkaline electrolytes and exhibit excellent OER activity. In 1 M KOH solution, the overpotentials at 10 mA cm⁻² are 135 mV (HER) and 243 mV (OER), respectively. The water splitting test demonstrates a low voltage requirement of only 1.51 V at 10 mA cm⁻², making it feasible to be powered by a standard 1.5 V commercial battery. The obtained results demonstrate superiority over commercially available noble metal catalysts as well as various catalysts reported in the literature. Furthermore, the catalysts exhibit excellent long-term stability in durability tests. Density flooding theory (DFT) calculations combined with XPS results confirm the existence of partial charge transfer from CoPt₃ to the substrate FeCoW oxide, and the excellent electrical conductivity makes CoPt₃/FCWO-NS essential to moderate the slow kinetics of the OER process. In addition, the substrate FeCoW oxide optimizes the position of the center of the d-band of CoPt₃, which makes CoPt₃/FCWO have suitable adsorption energy for hydrogen adsorption, which makes it possible to achieve efficient barrier-free HER under alkaline conditions.

2. Experimental

2.1. Materials

Sodium tungstate dihydrate (Na₂WO₄·2 H₂O; ≥99.5%), iron nitrate nonahydrate (Fe(NO₃)₃·9 H₂O; ≥ 99.0%), Cobalt nitrate hexahydrate (Co(NO₃)₂·6 H₂O; ≥ 99.0%), Chloroplatinic acid (H₂PtCl₆·3 H₂O), anhydrous ethanol (C₂H₅OH; ≥99.7%, CAS No.64-17-5) and isopropanol (C₃H₈O, CAS No.64-17) were purchased from Sinopharm Chemical Reagent Co., Ltd. Nafion solution (5%, CAS No. 31175-20-9), Ruthenium dioxide (RuO₂; CAS No. 12036-10-1) and acetylene black were purchased from Aladdin. Pt/C (20 wt%, HISPEC 30000) was purchased from Kunshan Yiersheng International Trade Co., LTD. The deionized water with 18.2 MΩ cm used in the experiments was purified by ZYPFT-2-20 T (Sichuan Excellence Water Treatment Equipment Co., Ltd.) system. Except for H₂PtCl₆, which requires ethanol solution preparation, the other products can be used directly without further purification.

2.2. Synthesis of catalysts

2.2.1. Synthesis of precursor

Precursor was prepared by a simple co-precipitation method. Dissolve 1 mmol Fe(NO₃)₃·9 H₂O and 2 mmol Co(NO₃)₂·6 H₂O in a mixture of 15 mL deionized water and 15 mL anhydrous ethanol with magnetic stirring for 30 min, and dissolve 3 mmol NaWO₄·2 H₂O in 30 mL deionized water with magnetic stirring for 30 min until completely dissolved. Then the sodium tungstate solution was added drop by drop to the mixed solution of Co and Fe salts while magnetic stirring for 2 h. It was then washed 5 times with deionized water at 8000 rpm, freeze-dried for 24 h, and then removed and recorded as the precursor.

2.2.2. Synthesis of Pt/a-FCWO-NP

The preparation method of Pt/a-FCWO-NP was the same as the precursor. After the sodium tungstate solution was added drop by drop to the mixed solution of Co and Fe salts while magnetic stirring for 2 h, about 5% of the total metal molar mass of H₂PtCl₆ solution was added, and then high purity N₂ was continuously injected while ultrasound. It was then washed 5 times with deionized water at 8000 rpm, freeze-dried for 24 h, and then removed and recorded as Pt/a-FCWO-NP.

2.2.3. Synthesis of crystalline a-FCWO-NS

The preparation method of a-FCWO-NS was the same as the precursor. After the sodium tungstate solution was added drop by drop to the mixed solution of Co and Fe salts while magnetic stirring for 2 h, 30 mL of fresh NaBH₄ solutions of 0.2 M, 0.4 M, and 0.6 M were added dropwise during high purity N₂ was continuously injected while ultrasound. They were then washed 5 times with deionized water at 8000 rpm, freeze-dried for 24 h, and then removed and recorded as a-FCWO-NS-1, a-FCWO-NS, and a-FCWO-NS-3, respectively.

2.2.4. Synthesis of CoPt₃/a-FCWO-NS

The preparation of CoPt₃/a-FCWO-NS was the same as the precursor. After the sodium tungstate solution was added drop by drop to the mixed solution of Co and Fe salts while magnetic stirring for 2 h, N₂ was continuously injected and 30 mL of 0.4 M fresh NaBH₄ solution was added dropwise while sonication. It was then washed 5 times with deionized water at 8000 rpm, freeze-dried for 24 h, and then removed and recorded as CoPt₃/a-FCWO-NS.

2.3. Characterization of materials

In this experiment, the X-ray diffraction of Rigaku D/MAX-3B type from Japan was used for the physical phase analysis of the synthesized materials. Cu K α radiation was used with a scan range of 10°– 90°, a scan rate of 4°/min and a voltage of 40 kV. FEI nova nanosem 450 field emission scanning electron microscope was used to analyze the material morphology as well as microstructure of the samples, where the resolution was 0.8 nm and the acceleration voltage was 40 kV. Talos F200X from Thermo Fisher Scientific was used to analyze the morphology, lattice striations, selected area electron diffraction (SAED), and elemental distribution of the material. Al/Mg was used as the double-anode target material, and the material was analyzed for elemental and valence analysis with a K-Alpha+ X-ray photoelectron spectrometer produced by Thermo Fisher Scientific Co. The specific surface area and pore size distribution of the materials were analyzed using NOVE2200e nitrogen adsorption BET surface from Conta, USA. The degassing temperature was 280 °C and the degassing time was 3 h. High-purity nitrogen (99.99%) was continuously introduced during the process at an operating temperature of 77 K. The pore size distribution of the material was determined using the NOVE2200e. The meteorological chromatograph was a GC97900II manufactured by Fuli Analytical Instrument Co.

2.4. Electrode preparation and electrochemical measurements

2.4.1. Preparation of electrodes

Prior to conducting the performance test, it is necessary to pretreat the rotating disc electrode (RDE) and nickel foam (NF). The RDE should undergo a polishing process using polishing powders of varying particle sizes on a chamois cloth. Subsequently, it should be thoroughly cleaned with deionized water and anhydrous ethanol before being utilized following the calibration test. A mixture comprising of a catalyst weighing 7 mg, acetylene black weighing 3 mg, deionized water measuring 490 μL , and isopropanol measuring 490 μL was prepared in a sealed container. Subsequently, the mixture was subjected to sonication for a duration of 30 min. Nafion (20 μL) was introduced into the solution, which was then subjected to continuous sonication for a duration of 30 min. Subsequently, 20 μL of the treated ink was carefully deposited onto the glassy carbon electrode surface and left to dry for a period of 12 h at ambient temperature. The nickel foam should be sequentially immersed in a 3 M HCl solution, deionized water, and an ethanol solution for 15 min of sonication. Subsequently, it should be infiltrated in an anhydrous ethanol solution and left to stand. The ink configuration utilized in the hydrolysis test remains consistent with the aforementioned procedure, however, it necessitates the deposition of 200 μL of ink onto nickel foam, followed by air drying at ambient conditions for a duration of 12 h prior to conducting the hydrolysis test.

2.4.2. Performance parameter

All performance tests were performed on a CHI 760E electrochemical workstation with Hg/HgO electrode as the reference electrode and platinum wire or platinum sheet as the counter electrode for the three-electrode system. Before the oxygen evolution reaction (OER) and hydrogen evolution reaction (HER) tests, it is necessary to continuously pass high-purity nitrogen (99.99%) in an electrolyte of 1 M KOH for 30 min and continuously pass nitrogen during the tests. LSV curves from 0.2 to 0.8 V (relative to Hg/HgO) were acquired in the OER at a scan rate of 5 mV/s at 1600 rpm (with 90% automatic iR compensation). LSV curves from -0.9 V to -1.5 V (relative to Hg/HgO) were acquired at a scan rate of 5 mV/s during HER (with 90% automatic iR compensation) at 1600 rpm. Electrochemical impedance spectroscopy (EIS) was recorded in the range of 100 kHz to 0.01 Hz with a test voltage of 10 mA cm^{-2} of potential and an amplitude of 10 mV. All potentials reported in this thesis were converted using a reversible hydrogen electrode (RHE), using the Nernst equation: $E_{\text{RHE}} = E_{\text{Hg/HgO}} + 0.059 \times \text{pH} + 0.098 \text{ V}$. The overpotential is calculated from the LSV curve obtained by the relationship, Overpotential = $E_{\text{RHE}} - 1.23 \text{ V}$.

2.5. Density functional theory (DFT)

The first-principle [27,28] was used to perform all density generalized function theory (DFT) calculations using the Perdew-Burke-Ernzerhof (PBE) [29] formulation in the generalized gradient approximation (GGA). The projection augmentation wave (PAW) potential [30,31] was chosen to describe the ion nuclei and a plane wave basis set with a kinetic energy cutoff of 520 eV was used to consider the valence electrons. The use of a Gaussian Blur method with a width of 0.05 eV allows for the partial occupation of the Kohn-Sham orbitals. When the energy change is less than 10–5 eV, the electron energy is considered to be self-consistent. The geometric optimization is considered convergent when the energy change is less than 0.05 eV \AA^{-1} . The vacuum spacing in the direction perpendicular to the structure plane was 18 \AA . The Brillouin region was integrated using $2 \times 2 \times 1$ Monkhorst-Pack k-point sampling for the structure. Finally, the adsorption energy E_{ads} is calculated as $E_{\text{ads}} = E_{\text{ad/sub}} - E_{\text{ad}} - E_{\text{sub}}$, where $E_{\text{ad/sub}}$, E_{ad} , and E_{sub} are the total energy of the optimized adsorbate/substrate system, the adsorbate in the structure, and the clean substrate, respectively. The free energy is calculated as:

$$G = E_{\text{ads}} + ZPE \cdot TS$$

where G , E_{ads} , ZPE , and TS are the free energy, DFT calculated total energy, zero-point energy, and entropy contribution, respectively.

3. Results and discussion

3.1. Characterization of samples

Fig. 1 illustrates the procedure for preparing Pt/a-FCWO-NP, CoPt₃/a-FCWO-NS, and a-FCWO-NS. The FeCoW oxide were initially synthesized using a straightforward co-precipitation technique. The CoPt₃/a-FCWO-NS with porous ultrathin nanosheets were synthesized through the introduction of nitrogen and the incorporation of NaBH₄ under sonication. The a-FCWO-NS catalyst was prepared without the addition of H₂PtCl₆, while the Pt/a-FCWO-NP catalyst was prepared without the addition of NaBH₄, using the same method for comparison purposes.

By studying the influence of NaBH₄ on the structural morphology and properties of materials, the optimal concentration of NaBH₄ was explored. From the XRD results in **Fig. S1**, the addition of NaBH₄ does not affect the amorphous structure of the precursor material, and the absence of significant peak changes after increasing the NaBH₄ concentration indicates that a new crystalline structure does not appear. The SEM results in **Fig. S2** show that the addition of NaBH₄ leads to the transformation of agglomerated nanoparticles into three-dimensional porous nanosheets. This is caused by the etching of NaBH₄, and some of the particles extend into ultra-thin nanosheets. The release of bubbles during the process of sonication plays a crucial role in promoting the formation of porous structures. Simultaneously, the presence of unetched nanoparticles effectively mitigates the risk of excessive collapse of the nanosheets. The investigation delved into the impact of varying concentrations of NaBH₄ on the properties of the precursor. The LSV results presented in **Fig. S3** demonstrate that the a-FCWO-NS catalyst exhibits the lowest overpotential for both OER and HER at 10 mA cm^{-2} , with values of 239 mV and 281 mV, respectively. Combining the aforementioned findings, it can be inferred that the performance of the catalyst is not affected by its structure, but rather by its morphology. The morphology of the prepared a-FCWO-NS exhibits optimal catalytic performance when the ratio of the total metal concentration (Fe+Co+W) to the concentration of NaBH₄ is 1:2. The process of transitional etching is expected to induce structural collapse, leading to a subsequent decrease in catalytic activity. However, the presence of certain nanoparticles alongside the nanosheets is anticipated to contribute positively to the overall stability of the nanostructure. Consequently, the CoPt₃/a-FCWO-NS was prepared using an identical NaBH₄ concentration.

The XRD pattern depicted in **Fig. 2a** does not exhibit any notable diffraction peaks for Pt/a-FCWO-NP. This observation suggests that the introduction of H₂PtCl₆ alone does not result in the formation of a distinct crystalline phase. The introduction of H₂PtCl₆, followed by NaBH₄, to the sample resulted in the formation of a limited quantity of CoPt₃ through the coordination of Co with Pt (PDF#29-0499) [32]. At a 20 angle of 40.5°, 47.1°, and 68.8°, the corresponding crystal planes of CoPt₃ are (111), (200), and (220), respectively. The XPS analysis depicted in **Fig. 2b** reveals the presence of significant amounts of Fe, Co, W, and O elements on the surface of the catalyst. Conversely, lower concentrations of B and Pt elements are observed (**Table S1**), and minimal Pt peaks are detected in Pt/a-FCWO-NP. The analysis of the surface elemental content of the samples, in conjunction with the results obtained from EDS and XPS as shown in **Fig. 2c**, demonstrates that the findings align with the elemental addition ratio. This suggests that the inclusion of NaBH₄ during sonication is advantageous for the formation of the CoPt₃, thereby preventing the depletion of Pt.

The SEM results, as depicted in **Fig. S4** and **Fig. 2d**, demonstrate the transition from nanoparticles to porous nanosheets following the introduction of NaBH₄. The morphologies of a-FCWO-NS and CoPt₃/a-

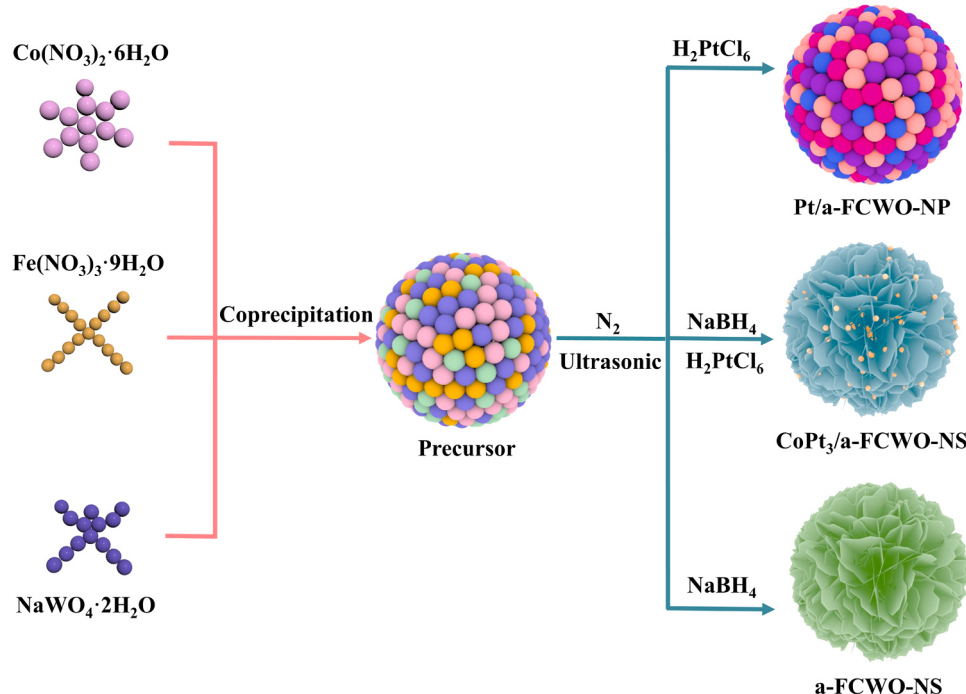


Fig. 1. The preparing procedures of Pt/a-FCWO-NP, CoPt₃/a-FCWO-NS and a-FCWO-NS.

FCWO-NS exhibit similarity, suggesting that the introduction of H₂PtCl₆ does not exert a substantial influence on morphology and result in collapse. The TEM results depicted in Fig. S5a, b indicates that the Pt/a-FCWO-NP structure is formed through the aggregation of nanoparticles, corroborating the findings from the SEM analysis. The high magnification transmission electron microscopy results in Fig. S5c reveal the absence of distinct lattice stripes in Pt/a-FCWO-NP. Additionally, the Fourier transformation (Fig. S5d) does not reveal any distinguishable diffraction rings, indicating the amorphous characteristics of Pt/a-FCWO-NP. The obtained result aligns with the XRD findings. Fig. S6 presents the dark field surface sweep of Pt/a-FCWO-NP, revealing a uniform distribution of Fe, Co, W, O, and Pt on the surface. The TEM results depicted in Fig. 2e, f demonstrate that CoPt₃/a-FCWO-NS displays ultrathin nanosheets that bear resemblance to monolayer graphene. The high magnification transmission electron microscopy results presented in Fig. 2g demonstrate the presence of both crystalline and amorphous phases in CoPt₃/a-FCWO-NS. Particle size analysis was conducted on the crystallized fraction, and the obtained results, as depicted in Fig. 2h, indicate that the average diameter of the crystallized CoPt₃ alloy is a mere 2.42 nm. After performing a Fourier transformation on the region in Fig. 2g where no clear lattice stripes are observed, Fig. 2i does not exhibit any distinct diffraction rings. This observation indicates the existence of a partially amorphous phase within the CoPt₃/a-FCWO-NS, thereby providing confirmation of the concurrent presence of both crystalline and amorphous phases. The analysis of the lattice stripes data involved intercepting a portion of the crystalline-amorphous phase in Fig. 2j. The lattice spacing of 0.228 nm and 0.142 nm corresponded to the (111) and (220) crystal planes of the CoPt₃ material, respectively. Taken collectively, the findings demonstrate that the introduction of minute quantities of H₂PtCl₆, followed by the addition of NaBH₄, facilitates the development of a crystalline CoPt₃. Conversely, the presence of both crystalline CoPt₃ and amorphous a-FCWO leads to the formation of a crystalline-amorphous heterogeneous interface. This interface effectively enhances the rate of electron transfer between the interfaces. The dark field analysis of CoPt₃/a-FCWO-NS, as shown in Fig. 2k, reveals a uniform distribution of Fe, Co, W, O, and Pt elements on the surface of the catalytic material. Fig. S7 illustrates that

the morphologies of a-FCWO-NS and CoPt₃/a-FCWO-NS are identical, demonstrating the presence of both nanosheets and nanoparticles. Among them, the absence of obvious lattice streaks in HRTEM and the diffuse diffraction rings of SAED species further verify the amorphous nature of a-FCWO-NS in XRD. In addition, the morphology and elemental distribution results of a-FCWO-NS (Fig. S8) indicate that the samples that were not completely reduced by NaBH₄ primarily consist of Fe and Co, while the ultrathin nanosheets formed as a result of the addition of NaBH₄ mainly consist of W oxides. These combined morphological findings demonstrate that NaBH₄ effectively enhances the morphology of the precursors. The resulting three-dimensional nanosheet structure significantly increases the number of active sites in the catalytic material, and the porous morphology facilitates the release of oxygen and hydrogen during the water splitting. The variation in the specific surface area of the catalysts was further confirmed through the analysis of BET, as depicted in Fig. S9. All of the nitrogen adsorption-desorption isothermal curves exhibit type IV isothermal behavior. Fig. S9a shows that the specific surface area of Pt/a-FCWO-NP is 48.39 m² g⁻¹, and is consistent with the SEM as well as TEM observations, where particle aggregation is evident, mainly as stacked pores between nanoparticles. The addition of NaBH₄ in parallel with sonication resulted in an increase in the specific surface area of a-FCWO-NS (Fig. S9b) to 117.57 m² g⁻¹. The addition of H₂PtCl₆ resulted in a further increase in the specific surface area of CoPt₃/a-FCWO-NS, as depicted in Fig. S9c. The specific surface area reached 131.69 m² g⁻¹. The pore size distribution results depicted in Fig. S9d-f indicate that the three catalytic materials predominantly exhibit mesopores, which effectively facilitate the release of gases throughout the catalytic process [33]. The pores of a-FCWO-NS and CoPt₃/a-FCWO-NS are predominantly generated through the process of nanosheet folding, thereby resulting in an augmented effective catalytic specific surface area [34].

The chemical valence and surface electronic states of each element were also analyzed by XPS. The Fe 2p XPS image in Fig. 3a of the CoPt₃/a-FCWO-NS was subjected to deconvolution analysis. The deconvolution resulted in the identification of Fe²⁺ 2p_{3/2} and Fe²⁺ 2p_{1/2} peaks at 710.79 eV and 723.19 eV, respectively. Additionally, Fe³⁺ 2p_{3/2} and Fe³⁺ 2p_{1/2} peaks were observed at 713.67 eV and 725.77 eV,

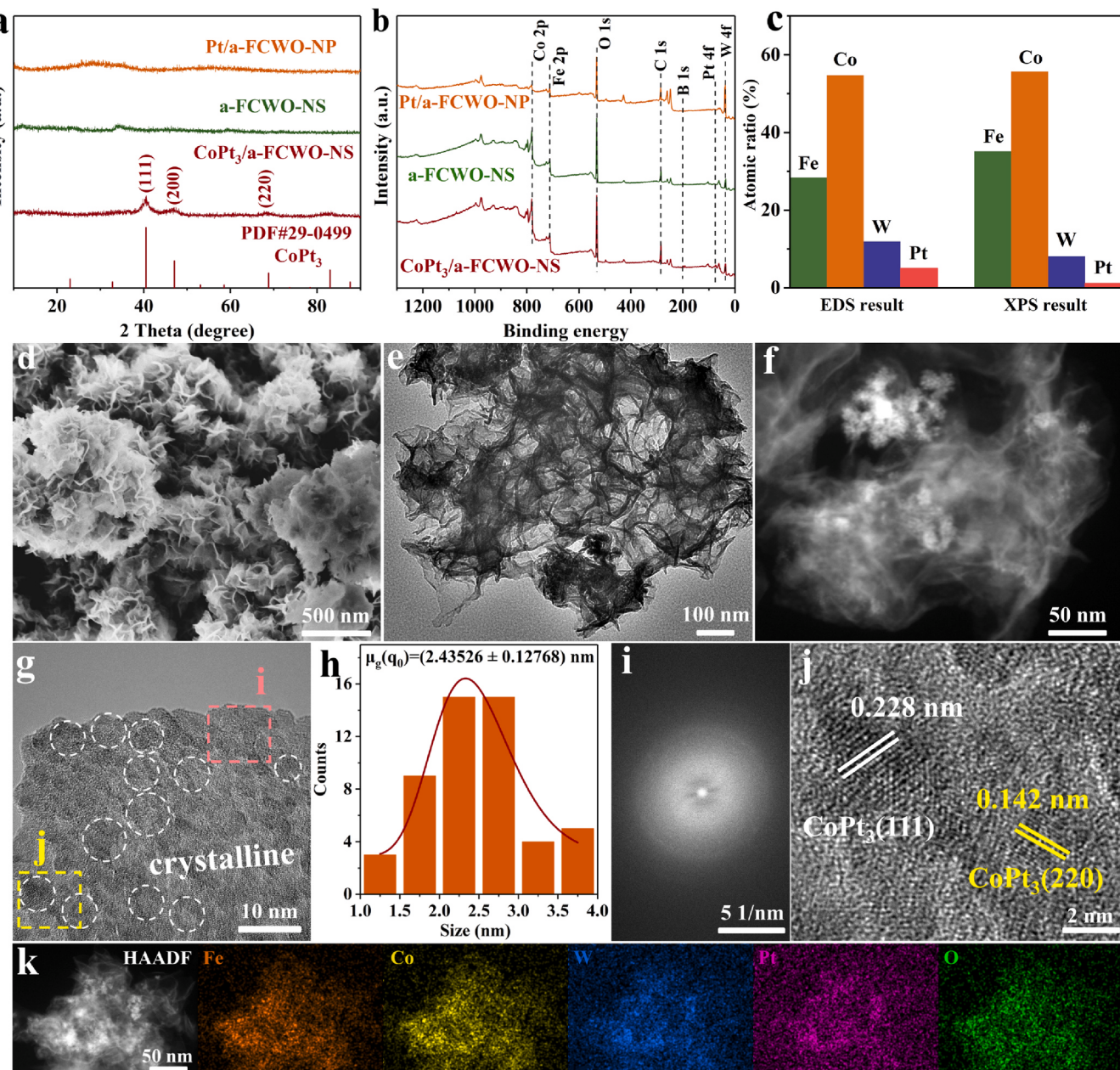


Fig. 2. (a) XRD image of Pt/a-FCWO-NP, a-FCWO-NS and CoPt₃/a-FCWO-NS. (b) XPS survey image of Pt/a-FCWO-NP, a-FCWO-NS and CoPt₃/a-FCWO-NS. (c) SEM images of CoPt₃/a-FCWO-NS. TEM images of CoPt₃/a-FCWO-NS at (e) low-magnification and (f) high-magnification, respectively. (g) HRTEM image of CoPt₃/a-FCWO-NS. (h) Diameter distribution of the crystalline part. (i) Fourier transform plot by HRTEM. (j) Magnification of the part from (g). (k) TEM image of a-FCWO-NS in dark field, and the corresponding elemental distributions of Fe, Co, Pt, W and O.

respectively. Furthermore, satellite peaks were detected at 716.49 eV, 719.45 eV, 729.48 eV, and 733.49 eV. Eight distinct peaks were observed in the Co 2p (Fig. 3b) for CoPt₃/a-FCWO-NS. The peaks at 780.44 eV and 796.33 eV were identified as Co³⁺ 2p_{3/2} and Co³⁺ 2p_{1/2}, respectively. Similarly, the peaks at 782.82 eV and 797.99 eV were attributed to Co²⁺ 2p_{3/2} and Co²⁺ 2p_{1/2}, while the peaks at 777.43 eV and 794.69 eV were assigned to Co⁰ 2p_{3/2} and Co⁰ 2p_{1/2}. The remaining four peaks were determined to be satellite peaks. The observed binding energies of W 4f in CoPt₃/a-FCWO-NS at 35.50 eV, 37.64 eV, and 40.61 eV can be attributed to the W 4f_{7/2}, W 4f_{5/2}, and loss feature, respectively (Fig. 3c). By comparing the binding energies of Fe 2p, Co 2p, and W 4f in the three samples, it is evident that CoPt₃/a-FCWO-NS exhibits a lower binding energy compared to a-FCWO-NS. This observation suggests that CoPt₃ transfers electrons to the carrier a-FCWO-NS following the formation of CoPt₃ on the surface of a-FCWO-NS.

Nevertheless, Pt/a-FCWO-NS exhibits a lower binding energy shift in Fe 2p compared to a-FCWO-NS, while both Co 2p and W 4 f experience a higher binding energy shift [35,36]. This observation suggests that the transfer of electrons in Pt/a-FCWO-NS is limited to Fe in the carrier a-FCWO-NS, whereas Co and W in a-FCWO-NS are responsible for transferring electrons to Pt. As described by the "ensemble effect" [37], the electron transfer between CoPt₃ and a-FCWO results in CoPt₃ becoming electron-poor, while a-FCWO becomes electron-rich [38]. The electron transfer occurring at the interfaces between different phases enhances the intrinsic activity of the catalyst, thereby promoting the adsorption of oxygen-containing intermediates by the catalytic species. Pt 4 f (Fig. 3d) displays the presence of peaks at 71.30 eV and 74.51 eV in CoPt₃/a-FCWO-NS, indicating the presence of Pt⁰. The presence of CoPt₃ on the surface of a-FCWO in the form of an alloy is indicated by the combined results of Co 2p and Pt 4 f. This alloy formation is

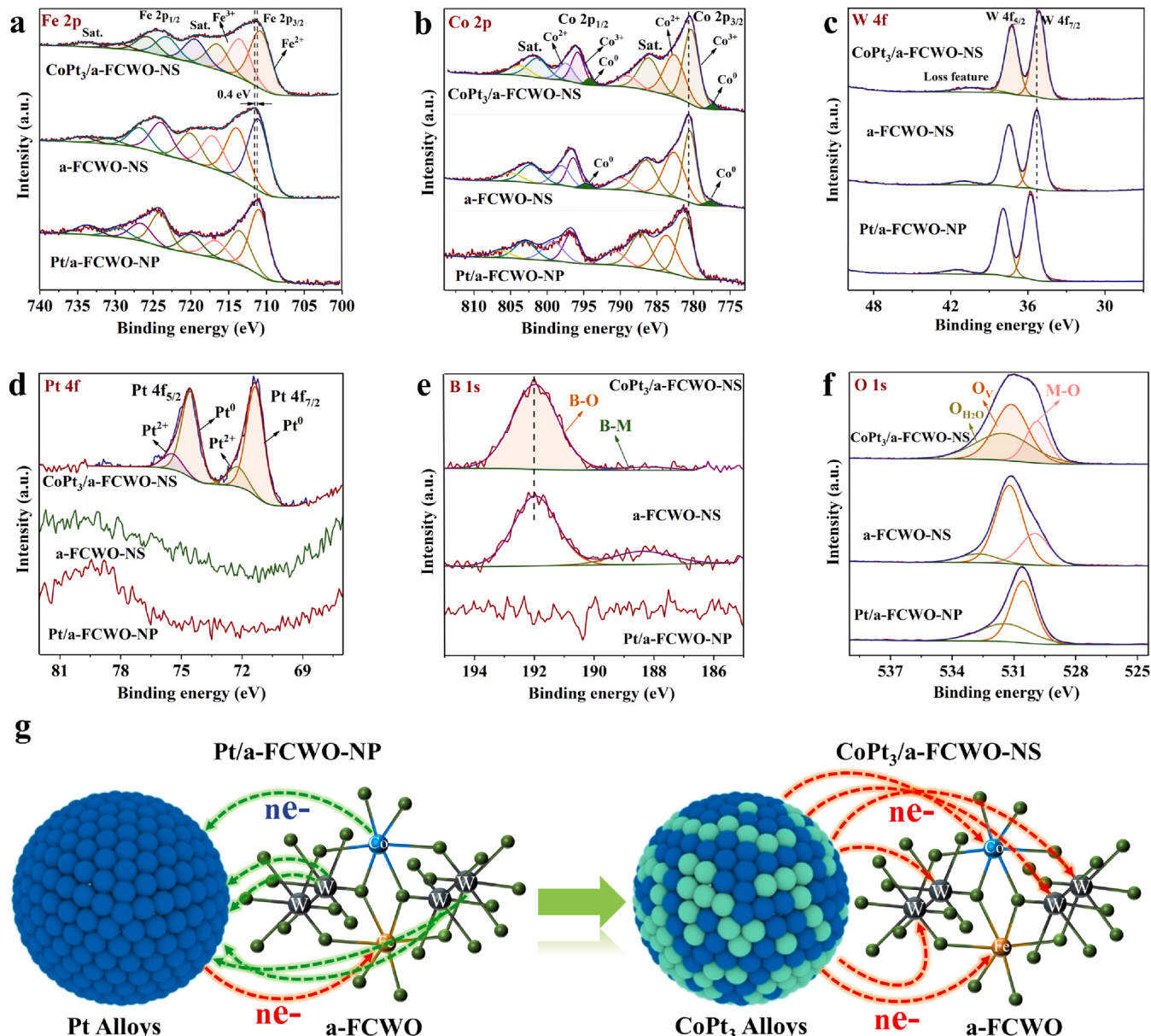


Fig. 3. XPS image of Pt/a-FCWO-NP, a-FCWO-NS and CoPt₃/a-FCWO-NS: (a) Fe 2p, (b) Co 2p, (c) W 4 f, (d) Pt 4 f, (e) B 1 s, (f) O 1 s (g) Schematic diagrams of electron transfer for Pt/a-FCWO-NP and CoPt₃/a-FCWO-NS.

primarily attributed to the reduction of NaBH₄. The observed peaks at 72.20 eV and 75.41 eV can be attributed to the presence of Pt²⁺. This finding also demonstrates that the Pt 4 f peak of Pt/a-FCWO-NP cannot be detected by XPS, suggesting that the utilization of NaBH₄ during sonication can significantly enhance the Pt loading rate. From the B 1 s spectrum (Fig. 3e), it can be observed that the boron in CoPt₃/a-FCWO-NS is predominantly in the form of B-O (191.96 eV), with a lesser presence of B-M (188.23 eV). The B 1 s peak position of a-FCWO-NS is identical to that of CoPt₃/a-FCWO-NS, while Pt/a-FCWO-NP is unable to detect the B peak. From the O 1 s spectrum (Fig. 3f), it can be observed that there is adsorbed water (531.46 eV) on the surface of CoPt₃/a-FCWO-NS. Additionally, the peaks at 531.12 eV and 529.87 eV are indicative of oxygen vacancies and M-O oxygen bonds [39], respectively. Fig. 3g illustrates the schematic representation of electron transfer in Pt/a-FCWO-NP and CoPt₃/a-FCWO-NS.

3.2. Electrochemical performance test of HER and OER

The performance was evaluated for the HER and OER using a three-electrode system in a 1 M KOH solution. The results of the LSV curve, as depicted in Fig. 4a, demonstrate that the overpotential of CoPt₃/a-FCWO-NS with a crystalline-amorphous heterostructure is merely 135 mV at 10 mA cm⁻². This value is significantly lower, by 219 mV, compared to that of Pt/a-FCWO-NP. This finding demonstrates a lower voltage of CoPt₃/a-FCWO-NS compared to the 281 mV observed for a-FCWO-NS, and it is in proximity to the 54 mV achieved using the commercially available noble metal catalyst Pt/C. The evaluation of the reaction kinetics in the HER process was also conducted based on the LSV data results. As depicted in Fig. 4b, the Tafel slope of CoPt₃/a-FCWO-NS is measured to be 80.69 mV dec⁻¹, indicating a higher rate of reaction kinetics compared to a-FCWO-NS (92.61 mV dec⁻¹) and Pt/a-FCWO-NP (118.24 mV dec⁻¹) [40]. The overpotential and Tafel slope of each catalyst at 10 mA cm⁻² are presented as dotted line plots in Fig. 4c. The findings indicate that CoPt₃/a-FCWO-NS exhibits the

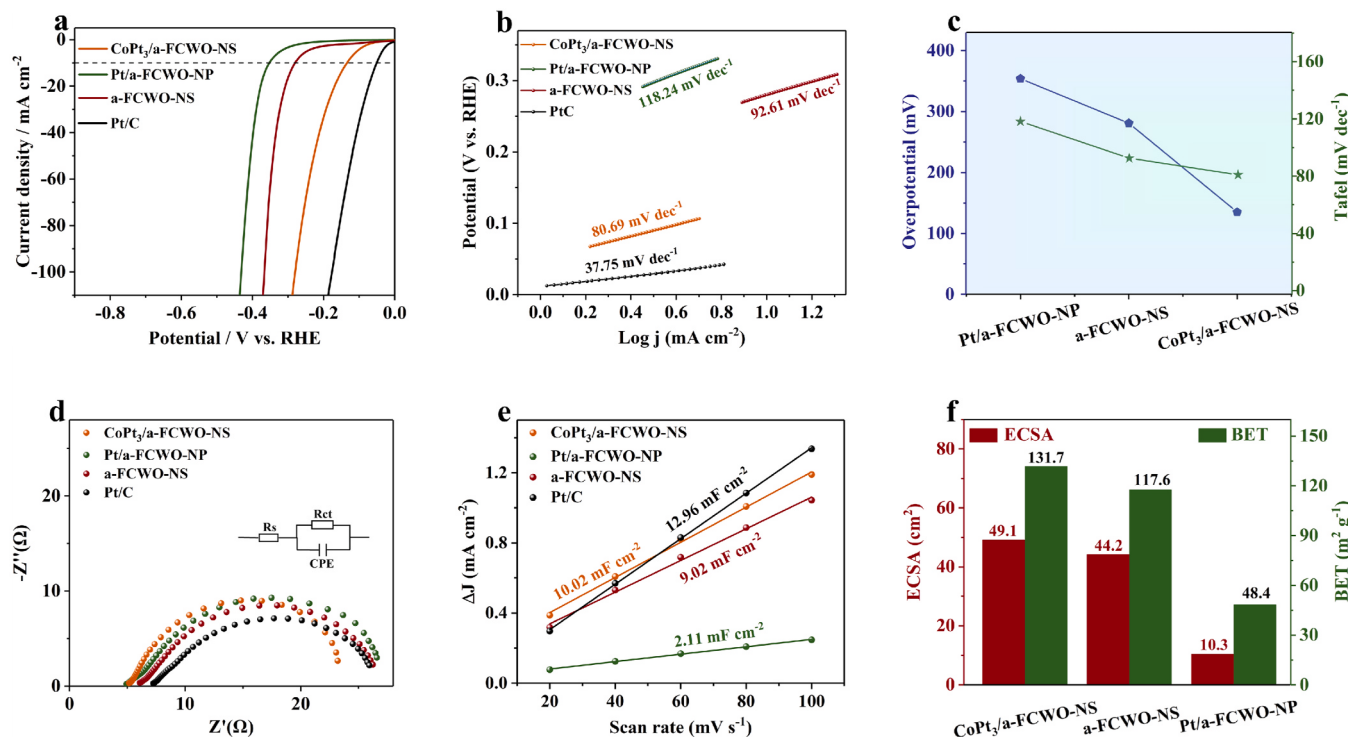


Fig. 4. (a) LSV curves of CoPt₃/a-FCWO-NS, Pt/a-FCWO-NP, a-FCWO-NS and Pt/C in 1 M KOH. (b) Tafel curve fitted according to LSV curve. (c) Comparison of overpotential at 10 mA cm⁻² and Tafel slope. (d) Nyquist diagram. (e) C_{dl} value fitted according to CV curves. (f) Histograms of electrochemically active surface area (ECSA) and BET.

highest HER performance. The verification of the reaction kinetics was conducted using EIS. The results, obtained after simulating the equivalent circuit, are presented in Fig. 4d. It can be observed that the CoPt₃/a-FCWO-NS, characterized by a crystalline-amorphous heterogeneous structure, exhibits a higher electron transfer rate [41]. The evaluation of electrochemical double-layer capacitance values was conducted in the non-faradaic reaction region (Fig. S10). The calculated results are presented in Fig. 4e, indicating a C_{dl} value of 10.02 mF cm⁻² for CoPt₃/a-FCWO-NS. Smaller values of 9.02 mF cm⁻² and 2.11 mF cm⁻² were obtained for a-FCWO-NS and Pt/a-FCWO-NP, respectively [42,43]. The detailed data are listed in Table S2. As depicted in Fig. 4f, the correlation between the electrochemical specific surface area and the specific surface area, as evidenced by the BET results, demonstrates a positive trend. This finding suggests that the introduction of ultrathin porous nanosheets through the ultrasonic addition of NaBH₄ can enhance the effective catalytic specific surface area. Based on the elemental analysis of XPS, the LSV curves were normalized in order to determine the turnover frequency (TOF) during the HER process. The results are shown in Fig. S11a, where CoPt₃/a-FCWO-NS has the highest TOF at the same voltage, which proves its intrinsic activity is the largest. In addition, the evaluation of stability is quite important for the availability of the catalyst. As depicted in Fig. S11b, the LSV curve following 5000 CV cycles exhibited a mere 8 mV decrease in overpotential at 10 mA cm⁻², suggesting that the catalyst demonstrates robust resistance to degradation. The HRTEM results presented in Fig. S12b demonstrate the coexistence of crystalline and amorphous phases in the CoPt₃/a-FCWO-NS material. Upon closer examination, the magnified view in Fig. S12c reveals that the lattice stripes observed correspond to the (200) and (111) crystal planes of CoPt₃. Additionally, the diffraction rings obtained from Fourier transformation (Fig. S12d) correspond to the (211), (110), and (111) crystal planes of CoPt₃. The elemental distribution results in Fig. S12e show that Pt maintains a high dispersion, indicating that CoPt₃ is stably enriched on the surface of a-FCWO-NS. The XPS (Fig. S13) results after the stability test show that the peaks of W

and B are not easily observed. This is primarily due to their dispersion in the electrolyte as tungsten and boron oxides. Fig. S13b shows that the Fe content becomes less than before the cycle. The Co 2p and Pt 4f results depicted in Fig. S13c, e demonstrates the continued presence of Co⁰ and Pt⁰, suggesting that CoPt₃ remains stable on the surface of a-FCWO. The aforementioned findings indicate that the catalyst successfully retains its ultrathin nanosheet morphology even after undergoing the stability test. Furthermore, the CoPt₃/a-FCWO structure remains stable and exhibits minimal changes throughout the reaction.

In addition to demonstrating exceptional performance in the HER, the OER performance in the identical electrolyte solution is also outstanding. The results of the LSV curve in Fig. 5a indicate that the overpotential of CoPt₃/a-FCWO-NS at 10 mA cm⁻² is 243 mV, slightly higher than that of a-FCWO-NS (239 mV). However, both CoPt₃/a-FCWO-NS and a-FCWO-NS exhibit the same overpotential at higher current densities and outperform Pt/a-FCWO-NP (258 mV). In contrast, the OER performance was observed to surpass that of RuO₂ at 378 mV. Fig. 5b depicts the Tafel slope values, which demonstrate a significant degree of proximity. Specifically, the CoPt₃/a-FCWO-NS (42.86 mV dec⁻¹) demonstrates a lower value in comparison to both a-FCWO-NS (43.68 mV dec⁻¹) and Pt/a-FCWO-NP (47.39 mV dec⁻¹), while also exhibiting a significantly lower value than RuO₂ (65.51 mV dec⁻¹). The results indicate that CoPt₃/a-FCWO-NS with a crystalline-amorphous heterogeneous structure has the fastest reaction kinetics under the same conditions. Fig. 5c presents the overpotential values of each catalyst at 10 mA cm⁻², along with the Tafel slope, represented as a histogram. The semicircle diameter in Fig. 5d, which is the smallest, suggests that CoPt₃/a-FCWO-NS exhibits the lowest resistance value. Furthermore, the resistance value of 8.72 Ω indicates that it possesses the highest electron transfer rate compared to all other catalysts. The CV experiment was conducted in the non-faradaic reaction region using various scan rates (Fig. (S14)) in order to ascertain the C_{dl} value. Fig. 5e illustrates that the CoPt₃/a-FCWO-NS exhibits a C_{dl} value of 43.37 mF cm⁻², which is comparable to that of a-FCWO-NS (37.63 mF cm⁻²), but

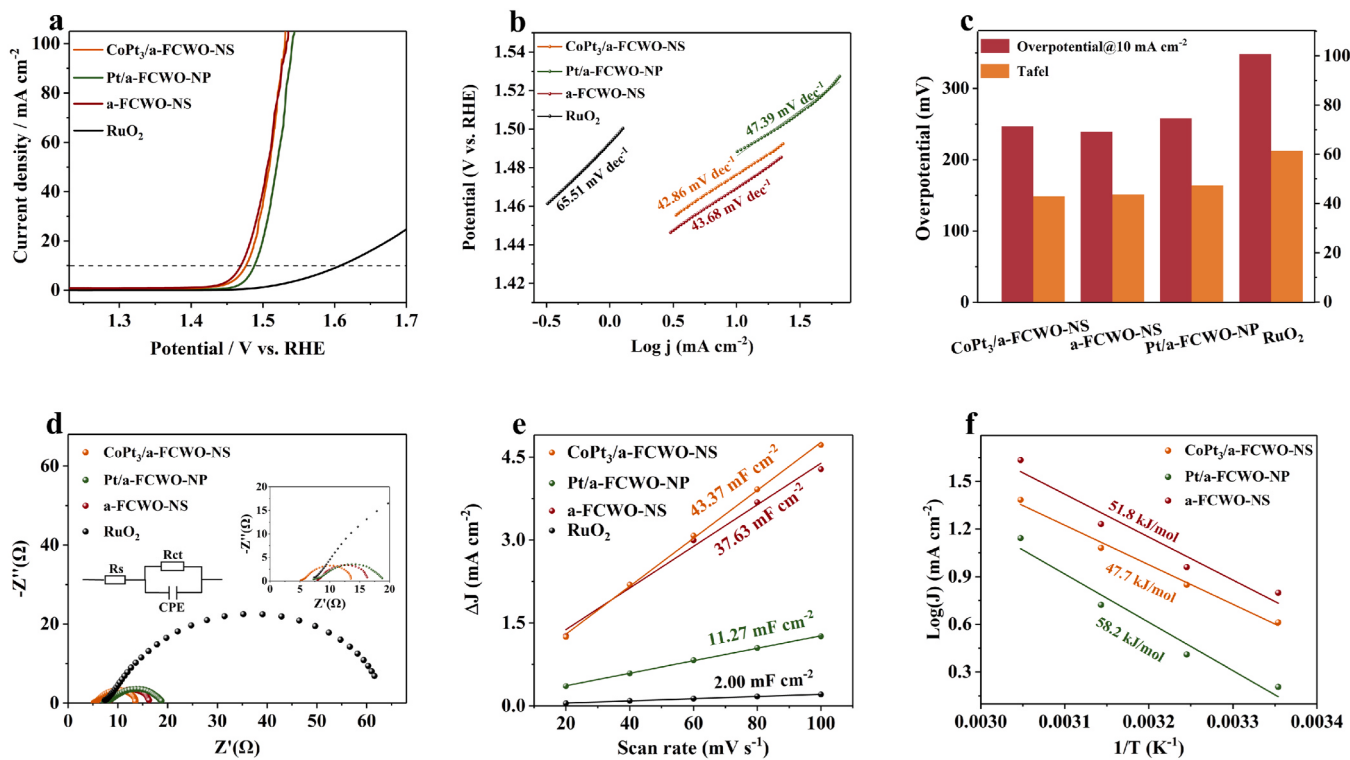


Fig. 5. (a) LSV curves of CoPt₃/a-FCWO-NS, Pt/a-FCWO-NP, a-FCWO-NS, and Pt/C in 1 M KOH. (b) Tafel curve fitted according to LSV curve. (c) Comparison of overpotential at 10 mA cm⁻² and Tafel slope. (d) Nyquist diagram, where the embedded plots are local zooms. (e) C_{dl} value fitted according to CV curves. (f) Arrhenius plot of inverse temperature for calculating activation energies of OER kinetics at 1.46 V (vs.RHE).

notably higher than Pt/a-FCWO-NP (11.27 mF cm⁻²). This observation suggests a strong correlation between the number of catalytic active sites and the fluffy structure of the material. In addition, the LSV curves (Fig. S15) were examined at various temperatures ranging from 25 °C to 55 °C in order to assess their reaction activation energy. The results are presented in Fig. 5f, and the comparison was conducted at a potential of 1.46 V (vs. RHE). It was observed that CoPt₃/a-FCWO-NS exhibited the lowest reaction activation energy of 47.7 kJ mol⁻¹, which is lower than that of a-FCWO-NS (51.8 kJ mol⁻¹) and a-FCWO (58.2 kJ mol⁻¹). It has been demonstrated that the CoPt₃/a-FCWO-NS material, characterized by a crystalline-amorphous structure, exhibits the lowest energy requirement for overcoming the OER under identical conditions. Additionally, this material facilitates the reaction more readily [44,45]. Taken collectively, the findings indicate that the influence of Pt loading on the performance of the OER is not readily discernible. Conversely, the augmentation of catalytic active sites resulting from the introduction of NaBH₄ is deemed more significant in terms of catalyst performance.

In addition, the potential of CoPt₃/a-FCWO-NS at 10 mA cm⁻² decreased by a mere 6 mV after 5000 cycles, as depicted in Fig. S16. This observation serves as evidence of the exceptional stability of the material in terms of OER [46]. The TEM results following the stability test for the reaction are depicted in Fig. S17a, demonstrating the preserved structure of the ultrathin nanosheets. The HRTEM results depicted in Fig. S17b reveal the coexistence of crystalline and amorphous phases. Furthermore, the magnified view in Fig. S17c demonstrates the presence of CoPt₃ crystal faces, specifically the (110) orientation, along with the observation of CoOOH crystal faces, including (121) and (140). The diffraction rings depicted in Fig. S17d illustrate the crystal planes (150), (120), (140), and (231) of CoOOH. These findings suggest that the OER primarily occurs through the conventional adsorption evolution mechanism (AEM) [47]. The elemental distribution results depicted in Fig. S17e demonstrate a uniform distribution of all elements across the surface. The XPS results after the OER stability test (Fig. S18) show that the W and B are dissolved in the electrolyte in the form of oxides [48].

The ratio of Co³⁺/Co²⁺ in Fig. S18c exhibited an increase from 1.35 to 1.42, suggesting the formation of CoOOH during the reaction [49]. This observation further supports the findings obtained from HRTEM analysis. The presence of Co⁰ and Pt⁰ in Fig. S18c, e equally demonstrates the stable enrichment of CoPt₃ on the surface of a-FCWO. The presence of MOO-H on the catalyst surface after stability testing, as indicated by the results of O 1 s in Fig. S18g, further confirms the formation of CoOOH [50]. Therefore, CoOOH is considered to be the real active center in the reaction.

3.3. Density functional theory (DFT) calculations

Density flooding theory (DFT) calculations were employed to conduct a comprehensive investigation into the charge difference, density of states, d-band center position, and adsorption energy on H₂O for these three structured materials. The aim was to explore the theoretical electrocatalytic mechanism in depth. Given the complexity of the amorphous FeCoW oxide structure, the crystalline CoWO₄ is employed as the foundational structure, with Fe substituting one Co atom to form FeCoW oxide. The Pt alloy is observed to be bonded to the Fe and O sites of FeCoW, while the CoPt₃ is directly attached to the Co, Fe, and O sites within the FeCoW structure. The structures depicted in Fig. S19a-c are the constructed a-FCWO, CoPt₃/a-FCWO, and Pt/a-FCWO, respectively.

The differential charge densities depicted in Fig. 6a-c indicate a partial charge transfer from Co to Fe in a-FCWO, as well as a partial charge transfer from Pt to a-FCWO in Pt/a-FCWO. The XPS results are supported by the presence of partial charge transfer from CoPt₃ to a-FCWO in the CoPt₃/a-FCWO system, as well as the observed increase in transferred electrons as indicated by the Bader charge quantization results.

The transfer of electrons across heterogeneous interfaces has the potential to enhance the intrinsic activity of catalysts, thereby promoting the adsorption of intermediates during the process of electrocatalytic water splitting [51]. The density of states (DOS) depicted in Fig. 6d-f

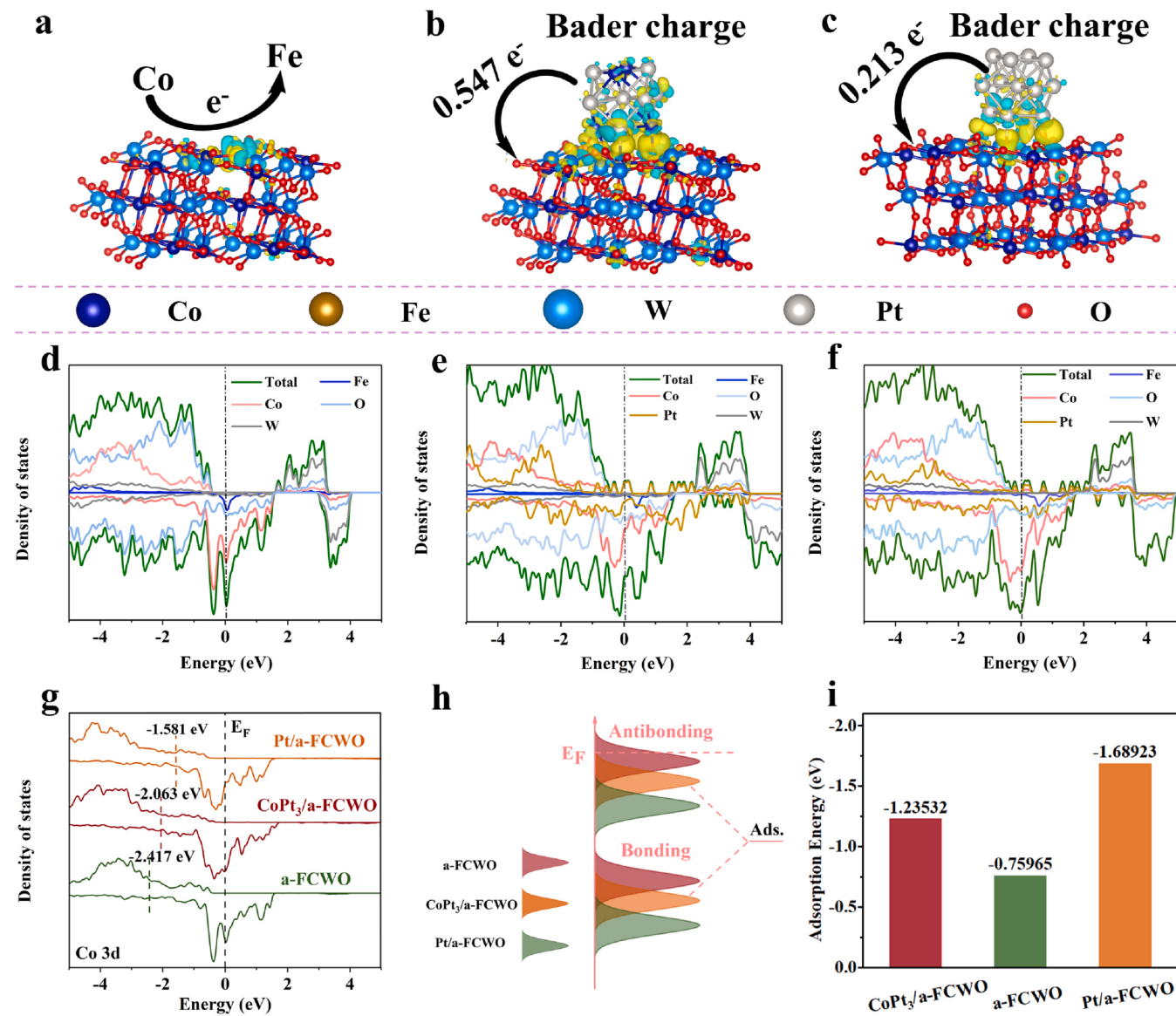


Fig. 6. Charge density difference of (a) a-FCWO, (b) CoPt₃/a-FCWO and (c) Pt/a-FCWO (The yellow and blue parts indicate the aggregation and depletion of the electrons, respectively). The total density of state: (d) a-FCWO, (e) Pt/a-FCWO and (f) CoPt₃/a-FCWO. (g) PDOS of Co 3d by a-FCWO, Pt/a-FCWO, and CoPt₃/a-FCWO. (h) Schematic illustration of bond formation between the catalyst surface and the adsorbates (Ads.). (i) Adsorption energy of H₂O molecules by CoPt₃/a-FCWO, a-FCWO and Pt/a-FCWO.

demonstrates that all three materials exhibit metallic properties, as evidenced by the crossing of the DOS with the Fermi energy level. This observation suggests that the materials possess excellent electrical conductivity, which in turn results in a lower mass transfer resistance during the catalytic process. In addition, it can be inferred that Co serves as the primary catalytically active center, as all electrons in close proximity to the Fermi energy level are contributed by the spin-down electrons of Co [52]. The correlation between the d-band position of Co and the Fermi energy level was further examined in order to ascertain the extent of adsorption and desorption capabilities of intermediates during the catalytic process. Both excessively high and excessively low d-band center positions have a negative impact on the OER. As shown in Fig. 6g, its d-band center position is calculated to be –2.063 eV, which is between –2.417 eV for a-FCWO and –1.581 eV for Pt/a-FCWO, and Co 3d in CoPt₃/a-FCWO has the most moderate d-band center position. As depicted in Fig. 6h, it can be observed that when the d-band center is in close proximity to the Fermi energy level, there is a stronger binding between the a-FCWO surface and the oxygen-containing intermediates.

This leads to a reduced electron filling rate in the antibonding orbital, resulting in excessive adsorption and hindered desorption. On the contrary, when the d-band centers are lower (Pt/a-FCWO), the binding to the intermediates becomes weak, resulting in reduced reactivity of the reaction [53]. The simulation also investigated the adsorption energy of H₂O with Co sites. The results, depicted in Fig. 6i, revealed that the adsorption energy of H₂O with all three catalysts was negative. This indicates an exothermic reaction and suggests that the catalytic active site can spontaneously adsorb H₂O molecules [54,55]. The adsorption energy of H₂O molecules on CoPt₃/a-FCWO is calculated to be –1.23532 eV, which falls within the range of –0.75965 eV for a-FCWO and –1.68923 eV for Pt/a-FCWO. The optimization of the d-band position of Co by Pt is primarily responsible for this phenomenon. Additionally, the CoPt₃/a-FCWO with a heterogeneous structure exhibits the most favorable adsorption energy for H₂O. This process will be more readily facilitated by the presence of water, which promotes the dissociation of H₂O molecules, resulting in an increased production of H₂.

3.4. Overall water splitting performance

The catalyst was immobilized onto a nickel foam substrate for comprehensive assessments of water splitting efficiency at both the cathode and anode, aiming to assess the catalyst's viability for practical implementation. The schematic diagram of the two-electrode test system is depicted in Fig. 7a. Prior to conducting the tests, the efficacy of an individual OER and HER was assessed using a three-electrode experimental setup. Fig. 7b demonstrates that the CoPt₃/a-FCWO-NS/NF outperforms the commercially available noble metal catalyst RuO₂ in the OER process, achieving a voltage of 1.435 V at 10 mA cm⁻². The performance of HER is comparable to that of Pt/C, as it exhibits a voltage of merely 0.075 V at 10 mA cm⁻². The results of the two-electrode test system are presented in Fig. 7c. It can be observed that the CoPt₃/a-FCWO-NS/NF double exhibits a voltage of only 1.51 V at 10 mA cm⁻², which is superior to both the Pt/C/NF//RuO₂/NF (1.52 V) and NF (1.84 V) configurations. This voltage necessitates the use of a single commercial battery with a voltage of 1.5 V to facilitate the water splitting process. The outcomes of this process can be observed in the supplementary video (Supplementary Information) and Fig. 7d. As depicted in Fig. 7e, the impedance test results indicate that the CoPt₃/a-FCWO-NS loaded on the NF demonstrates the lowest resistance value of merely

3.81 Ω after conducting the equivalent circuit simulation. This value is lower compared to the Pt/C/NF//RuO₂/NF with a resistance of 3.90 Ω and the NF with a resistance of 8.4 Ω. The current density in the two-electrode test system was observed to maintain its initial value of 93.6% after undergoing 100 h of time-current testing at a potential of 1.57 V. This testing was conducted in a 1 M KOH solution at room temperature. (Fig. 7f). However, the current density of the noble metal catalysts exhibited a significant decline after approximately 30 h, with the current density reaching only 84.6% of its initial value after 100 h. Fig. S22 shows the microscopic morphology of the material after the stability test, the overall morphology of the material did not change significantly and still maintained the structure of the nanosheet, indicating the stability of the structure of the material. In addition, the catalyst has a lower voltage at 10 mA cm⁻² than numerous reported catalysts (Fig. 7g and Table S4).

Supplementary material related to this article can be found online at doi:10.1016/j.apcatb.2023.123387.

The actual rate of release of hydrogen and oxygen produced by the catalyst and Faraday efficiency were likewise explored. Based on the real-time monitored gas chromatography (GC) test results, it was observed that the actual average H₂ and O₂ content ratio of 1.99, as depicted in Fig. S23 and Table S5. The Faraday test results depicted in

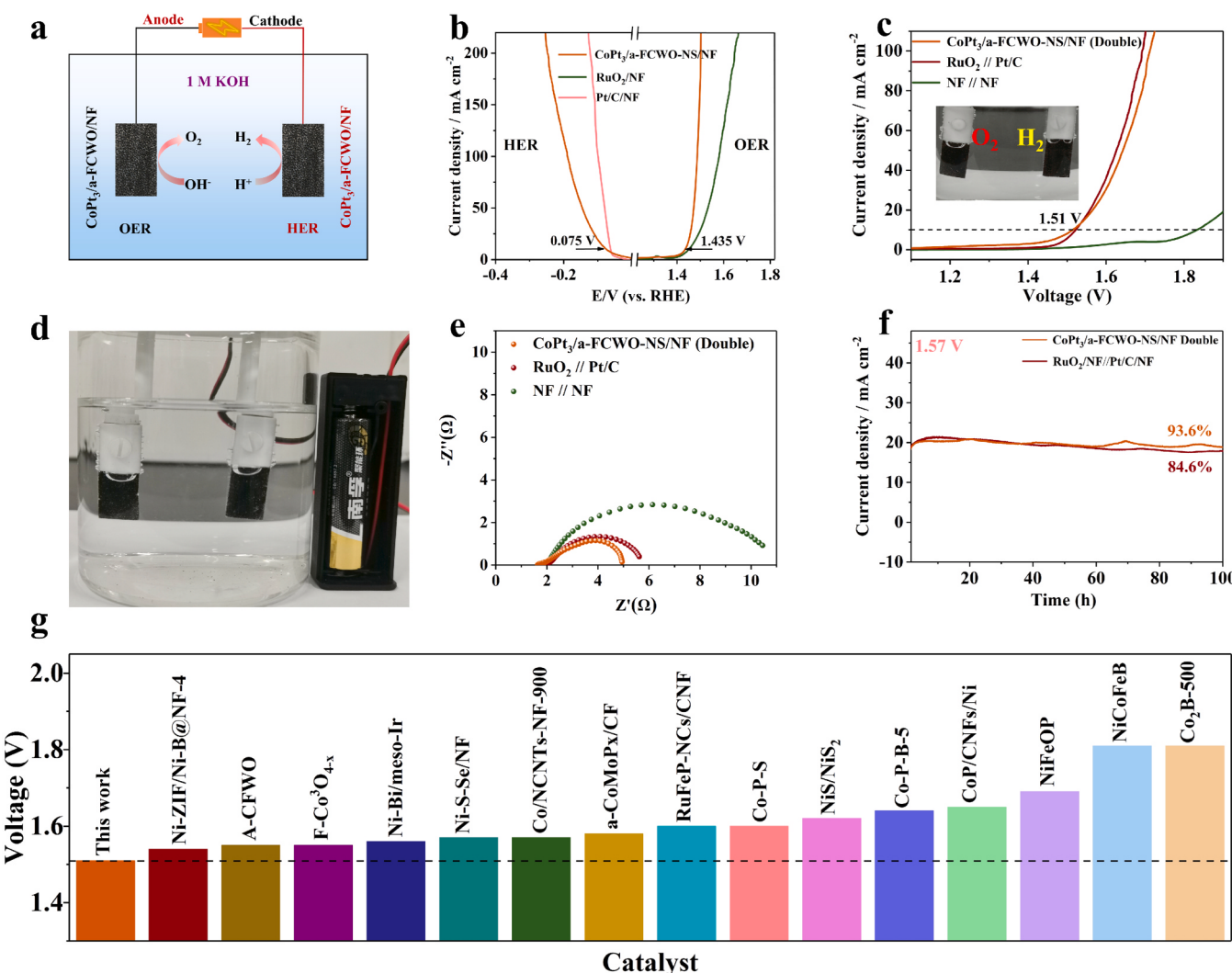


Fig. 7. (a) Schematic diagram of two-electrode system test for overall water splitting. (b) OER and HER polarization curve of CoPt₃/a-FCWO-NS/NF, RuO₂/NF, and Pt/C/NF. (c) The performance of overall water splitting of CoPt₃/a-FCWO-NS/NF = |CoPt₃/a-FCWO-NS/NF, RuO₂/NF = |Pt/C/NF and NF = |NF, where the embedded graph is the actual hydrolysis graph. (d) Actual drawing of electrolytic water using commercial 1.5 V battery. (e) Nyquist diagram of overall water splitting. (f) 100 h time-current density curve at 1.57 V. (g) Literature comparison on overall water splitting properties.

Fig. S24 demonstrate that the CoPt₃/a-FCWO-NS catalyst exhibited hydrogen and oxygen outputs of 42.2 mL/h and 20.7 mL/h at 100 mA cm⁻², respectively, with a nearly 2:1 ratio. The above results prove that Faraday's efficiency is close to 100% [56]. This finding serves as strong evidence that the catalysts possess the ability to selectively oxidize water into hydrogen and oxygen. Furthermore, the porous and heterogeneous structures of the catalysts work synergistically to enhance the catalytic activity for water decomposition, resulting in the highest observed efficiency. In conclusion, the performance of water splitting can be enhanced by the modification of the NF with CoPt₃/a-FCWO-NS, owing to its distinctive morphology and heterogeneous structure. Therefore, CoPt₃/a-FCWO-NS exhibits promising potential for future applications in water splitting.

4. Conclusions

In conclusion, the CoPt₃/a-FCWO-NS interfacial nanocatalyst demonstrates significant potential for future applications in water splitting. In this study, we present a novel interfacial nanocatalyst consisting of CoPt₃/a-FCWO-NS. The findings indicate that the arrangement of ultrathin nanosheets in a porous structure enhances the number of active sites available for catalytic reactions. Additionally, the presence of a crystalline-amorphous heterogeneous structure boosts the intrinsic activity of the catalyst, resulting in a highly efficient electrocatalytic water splitting process in alkaline environments. We demonstrate that there is a transfer of charge from crystalline CoPt₃ to amorphous a-FCWO. The synergistic interaction between CoPt₃ and amorphous a-FCWO also serves to optimize the d-band center of Co, thereby enhancing the adsorption strength of water and hydrogen sorbent. This optimization is crucial for the efficient process of water splitting. The results of the water splitting experiment demonstrate that 10 mA cm⁻² can be attained at a voltage of 1.51 V. Remarkably, this level of performance can be achieved using a standard commercial battery with a voltage of 1.5 V, which is sufficient to drive the overall water splitting process and generate both oxygen and hydrogen. The Faraday efficiency approaches nearly 100%. The catalytic performance of CoPt₃/a-FCWO-NS surpasses that of electrodes constructed using commercially available noble metal catalysts. The catalyst exhibits exceptional stability. This study presents novel concepts for the development of catalysts used in industrial water electrolysis, offering potential advancements for future designs.

CRediT authorship contribution statement

Zhenlong Wang: Investigation, Writing – original draft, Writing – review & editing, Data curation, Formal analysis. **Sirong Li:** Investigation, Data curation, Formal analysis, Software. **Guofei Zhang:** Investigation, Data curation, Formal analysis, Software. **Xin Yu:** Data curation, Formal analysis, Software. **Zhengyi Zhao:** Investigation, Data curation, Formal analysis. **Yipeng Zhang and Yang Shi:** Formal analysis, Software. **Xuechun Xiao and Hai-Bin Zhu:** Writing – review & editing, Supervision, Project administration, Funding acquisition, Resources.

Declaration of Competing Interest

The authors declare that they have no known competing financial interests or personal relationships that could have appeared to influence the work reported in this paper.

Data Availability

No data was used for the research described in the article.

Acknowledgments

Zhenlong Wang and Sirong Li contributed equally to this work. This work was supported by National Natural Science Foundation of China

(Grant No.61751107, No.22172025), the Science and Education Integration Open Project of Ningbo Institute of Materials Science, Chinese Academy of Sciences and Program for Innovative Research Team (in Science and Technology) in University of Yunnan Province and the Postgraduate Research and Innovation Foundation of Yunnan University (2021Y344).

Appendix A. Supporting information

Supplementary data associated with this article can be found in the online version at doi:10.1016/j.apcatb.2023.123387.

References

- [1] H. Yang, Z. Chen, P. Guo, B. Fei, R. Wu, B-doping-induced amorphization of LDH for large-current-density hydrogen evolution reaction, *Appl. Catal. B: Environ.* 261 (2020), 118240, <https://doi.org/10.1016/j.apcatb.2019.118240>.
- [2] H. Song, J. Yu, Z. Tang, B. Yang, S. Lu, Halogen-doped carbon dots on amorphous cobalt phosphide as robust electrocatalysts for overall water splitting, *Adv. Energy Mater.* 12 (2022) 2102573, <https://doi.org/10.1002/aenm.202102573>.
- [3] F. Tian, S. Geng, L. He, Y. Huang, A. Fauzi, W. Yang, Y. Liu, Y. Yu, Interface engineering: PSS-PPy wrapping amorphous Ni-Co-P for enhancing neutral-pH hydrogen evolution reaction performance, *Chem. Eng. J.* 417 (2021), 129232, <https://doi.org/10.1016/j.cej.2021.129232>.
- [4] X. Li, L. Xiao, L. Zhou, Q. Xu, J. Wang, J. Xu, B. Liu, Adaptive bifunctional electrocatalyst of amorphous CoFe oxide @ 2D black phosphorus for overall water splitting, *Angew. Chem. Int. Ed. Engl.* 59 (2020) 21106–21113, <https://doi.org/10.1002/anie.202008514>.
- [5] X. Luo, P. Ji, P. Wang, R. Cheng, D. Chen, C. Lin, J. Zhang, J. He, Z. Shi, N. Li, S. Xiao, S. Mu, Interface engineering of hierarchical branched Mo-doped Ni₃S₂/Ni₃P hollow heterostructure nanorods for efficient overall water splitting, *Adv. Energy Mater.* 10 (2020) 1903891, <https://doi.org/10.1002/aenm.201903891>.
- [6] J. Xu, C. Zhang, H. Liu, J. Sun, R. Xie, Y. Qiu, F. Lü, Y. Liu, L. Zhuo, X. Liu, J. Luo, Amorphous MoO_x-Stabilized single platinum atoms with ultrahigh mass activity for acidic hydrogen evolution, *Nano Energy* 70 (2020), 104529, <https://doi.org/10.1016/j.nanoen.2020.104529>.
- [7] Y. Wang, Q. Sun, Z. Wang, W. Xiao, Y. Fu, T. Ma, Z. Wu, L. Wang, In situ phase-reconfiguration to synthesize Ru, B co-doped nickel phosphide for energy-efficient hydrogen generation in alkaline electrolytes, *J. Mater. Chem. A* 10 (2022) 16236–16242, <https://doi.org/10.1039/dta02685f>.
- [8] W. Feng, Y. Feng, J. Chen, H. Wang, Y. Hu, T. Luo, C. Yuan, L. Cao, L. Feng, J. Huang, Interfacial electronic engineering of Ru/FeRu nanoparticles as efficient trifunctional electrocatalyst for overall water splitting and Zn-air battery, *Chem. Eng. J.* 437 (2022), 135456, <https://doi.org/10.1016/j.cej.2022.135456>.
- [9] M. Liu, H. Chun, T.C. Yang, S.J. Hong, C.M. Yang, B. Han, L.Y.S. Lee, Tuning the site-to-site interaction in Ru-M (M = Co, Fe, Ni) diatomic electrocatalysts to climb up the volcano plot of oxygen electroreduction, *ACS Nano* 16 (2022) 10657–10666, <https://doi.org/10.1021/acsnano.2c02324>.
- [10] Y. Zhou, Q. Gu, K. Yin, Y. Li, L. Tao, H. Tan, Y. Yang, S. Guo, Engineering eg orbital occupancy of Pt with Au alloying enables reversible Li-O₂ batteries, *Angew. Chem. Int. Ed. Engl.* 61 (2022), e202201416, <https://doi.org/10.1002/anie.202201416>.
- [11] J. Wang, L. Han, B. Huang, Q. Shao, H.L. Xin, X. Huang, Amorphization activated ruthenium-tellurium nanorods for efficient water splitting, *Nat. Commun.* 10 (2019) 5692, <https://doi.org/10.1038/s41467-019-13519-1>.
- [12] C. Zhang, Y. Cui, Y. Yang, L. Lu, S. Yu, Z. Meng, Y. Wu, Y. Li, Y. Wang, H. Tian, W. Zheng, Highly conductive amorphous pentlandite anchored with ultrafine platinum nanoparticles for efficient pH-universal hydrogen evolution reaction, *Adv. Funct. Mater.* 31 (2021) 2105372, <https://doi.org/10.1002/adfm.202105372>.
- [13] L. Liu, Y. Wang, Y. Zhao, Y. Wang, Z. Zhang, T. Wu, W. Qin, S. Liu, B. Jia, H. Wu, D. Zhang, X. Qu, M. Chhowalla, M. Qin, Ultrahigh Pt-mass-activity hydrogen evolution catalyst electrodeposited from bulk Pt, *Adv. Funct. Mater.* 32 (2022) 2112207, <https://doi.org/10.1002/adfm.202105372>.
- [14] Z. Cai, L. Li, Y. Zhang, Z. Yang, J. Yang, Y. Guo, L. Guo, Amorphous nanocages of Cu-Ni-Fe hydr(oxy)oxide prepared by photocorrosion for highly efficient oxygen evolution, *Angew. Chem. Int. Ed. Engl.* 58 (2019) 4189–4194, <https://doi.org/10.1002/anie.201812601>.
- [15] J. Wang, S. Xin, Y. Xiao, Z. Zhang, Z. Li, W. Zhang, C. Li, R. Bao, J. Peng, J. Yi, S. Chou, Manipulating the water dissociation electrocatalytic sites of bimetallic nickel-based alloys for highly efficient alkaline hydrogen evolution, *Angew. Chem. Int. Ed.* 61 (2022), e202202518, <https://doi.org/10.1002/anie.202202518>.
- [16] H. Zhang, J. Diao, M. Ouyang, H. Yadegari, M. Mao, M. Wang, G. Henkelman, F. Xie, D.J. Riley, Heterostructured core-shell Ni-Co@Fe-Co nanoboxes of prussian blue analogues for efficient electrocatalytic hydrogen evolution from alkaline seawater, *ACS Catal.* 13 (2023) 1349–1358, <https://doi.org/10.1021/acscatal.2c05433>.
- [17] M. Li, R. Sun, Y. Li, J. Jiang, W. Xu, H. Cong, S. Han, The 3D porous “celosia” heterogeneous interface engineering of layered double hydroxide and P-doped molybdenum oxide on MXene promotes overall water-splitting, *Chem. Eng. J.* 431 (2022), 133941, <https://doi.org/10.1016/j.cej.2021.133941>.
- [18] D.N. Nguyen, M. Fadel, P. Chenevier, V. Artero, P.D. Tran, Water-splitting artificial leaf based on a triple-junction silicon solar cell: one-step fabrication through

- photoinduced deposition of catalysts and electrochemical operando monitoring, *J. Am. Chem. Soc.* 144 (2022) 9651–9660, <https://doi.org/10.1021/jacs.2c00666>.
- [19] B. Zhang, X. Zheng, O. Voznyy, R. Comin, M. Bajdich, M.G. Melchor, L. Han, J. Xu, M. Liu, L. Zheng, F.P. Arquer, C. Dinh, F. Fan, M. Yuan, E. Yassitepe, N. Chen, T. Regier, P. Liu, Y. Li, P.D. Luna, A. Jammohamed, H.L. Xin, H. Yang, A. Vojvodic, E.H. Sargent, Homogeneously dispersed multimetal oxygen-evolving catalysts, *science* 352 (2016) 333–337, <https://doi.org/10.1126/science.aaf1525>.
- [20] W. Li, S. Watzele, H.A. El-Sayed, Y. Liang, G. Kieslich, A.S. Bandarenka, K. Rodewald, B. Rieger, R.A. Fischer, Unprecedented high oxygen evolution activity of electrocatalysts derived from surface-mounted metal-organic frameworks, *J. Am. Chem. Soc.* 141 (2019) 5926–5933, <https://doi.org/10.1021/jacs.9b00549>.
- [21] Z. Wang, S. Li, G. Zhang, X. Yu, Y. Shi, Y. Zhang, X. Xiao, Facile synthesis of FeCoW oxides: Effects of amorphous structure, electronic configuration and catalytic sites on water oxidation, *J. Alloy. Compd.* 933 (2023), 167787, <https://doi.org/10.1016/j.jallcom.2022.167787>.
- [22] C. Liu, J. Wang, J. Wan, Y. Cheng, R. Huang, C. Zhang, W. Hu, G. Wei, C. Yu, Amorphous metal-organic framework-dominated nanocomposites with both compositional and structural heterogeneity for oxygen evolution, *Angew. Chem. Int. Ed. Engl.* 59 (2020) 3630–3637, <https://doi.org/10.1002/anie.201914587>.
- [23] Y. Song, M. Song, P. Liu, W. Liu, L. Yuan, X. Hao, L. Pei, B. Xu, J. Guo, Z. Sun, Fe-doping induced localized amorphization in ultrathin α -Ni(OH)₂ nanomesh for superior oxygen evolution reaction catalysis, *J. Mater. Chem. A* 9 (2021) 14372–14380, <https://doi.org/10.1039/dta02341a>.
- [24] G. Wu, X. Zheng, P. Cui, H. Jiang, X. Wang, Y. Qu, W. Chen, Y. Lin, H. Li, X. Han, Y. Hu, P. Liu, Q. Zhang, J. Ge, Y. Yao, R. Sun, Y. Wu, L. Gu, X. Hong, Y. Li, A general synthesis approach for amorphous noble metal nanosheets, *Nat. Commun.* 10 (2019) 4855, <https://doi.org/10.1038/s41467-019-12859-2>.
- [25] D. Tran, V. Hoa, S. Prabhakaran, D. Kim, Activated CuNi@Ni Core@shell structures via oxygen and nitrogen dual coordination assembled on 3D CNTs-graphene hybrid for high-performance water splitting, *Appl. Catal. B: Environ.* 294 (2021), 120263, <https://doi.org/10.1016/j.apcatb.2023.122717>.
- [26] L. Ma, Z. Wei, C. Zhao, X. Meng, H. Zhang, M. Song, Y. Wang, B. Li, X. Huang, C. Xu, M. Feng, P. He, D. Ji, Y. Zhou, X. Duan, Hierarchical superhydrophilic/superaerophobic 3D porous trimetallic (Fe, Co, Ni) spinel/carbon/nickel foam for boosting oxygen evolution reaction, *Appl. Catal. B: Environ.* 332 (2023), 122717, <https://doi.org/10.1016/j.apcatb.2023.122717>.
- [27] G. Kresse, J. Furthmüller, Efficiency of ab-initio total energy calculations for metals and semiconductors using a plane-wave basis set, *Comput. Mater. Sci.* 6 (1996) 15–50, [https://doi.org/10.1016/0927-0256\(96\)00008-0](https://doi.org/10.1016/0927-0256(96)00008-0).
- [28] G. Kresse, J. Furthmüller, Efficient iterative schemes for ab initio total-energy calculations using a plane-wave basis set, *Phys. Rev. B* 54 (1996) 11169–11186, <https://doi.org/10.1103/PhysRevB.54.11169>.
- [29] J.P. Perdew, K. Burke, M. Ernzerhof, Generalized gradient approximation made simple, *Phys. Rev. Lett.* 77 (1996) 3865–3868, <https://doi.org/10.1103/PhysRevLett.77.3865>.
- [30] G. Kresse, D. Joubert, From ultrasoft pseudopotentials to the projector augmented-wave method, *Phys. Rev. B* 59 (1999) 1758–1775, <https://doi.org/10.1103/PhysRevB.59.1758>.
- [31] P.E. Blöchl, Projector augmented-wave method, *Phys. Rev. B* 50 (1994) 17953–17979, <https://doi.org/10.1103/PhysRevB.50.17953>.
- [32] Z. Lu, J. Xie, J. Hu, K. Wang, Y. Cao, In situ replacement synthesis of Co@NCNT encapsulated CoPt₃@Co₂P heterojunction boosting methanol oxidation and hydrogen evolution, *Small* 17 (2021), e2104656, <https://doi.org/10.1002/smll.202104656>.
- [33] P. Wang, Y. Luo, G. Zhang, Z. Chen, H. Ranganathan, S. Sun, Z. Shi, Interface engineering of Ni_xSY@MnO_xHy nanorods to efficiently enhance overall-water-splitting activity and stability, *Nano-Micro Lett.* 14 (2022) 120.
- [34] H. Xu, B. Fei, G. Cai, Y. Ha, J. Liu, H. Jia, J. Zhang, M. Liu, R. Wu, Boronization-induced ultrathin 2D nanosheets with abundant crystalline-amorphous phase boundary supported on nickel foam toward efficient water splitting, *Adv. Energy Mater.* 10 (2019) 1902714, <https://doi.org/10.1002/aenm.201902714>.
- [35] J. Chen, H. Li, Z. Pei, Q. Huang, Z. Yuan, C. Wang, X. Liao, G. Henkelman, Y. Chen, L. Wei, Catalytic activity atlas of ternary Co-Fe-V metal oxides for the oxygen evolution reaction, *J. Mater. Chem. A* 8 (2020) 15951–15961, <https://doi.org/10.1039/DOTA04088F>.
- [36] M. Kuang, J. Zhang, D. Liu, H. Tan, K.N. Dinh, L. Yang, H. Ren, W. Huang, W. Fang, J. Yao, X. Hao, J. Xu, C. Liu, L. Song, B. Liu, Q. Yan, Amorphous/Crystalline heterostructured cobalt-vanadium-iron (oxy)hydroxides for highly efficient oxygen evolution reaction, *Adv. Energy Mater.* 10 (2020) 2002215, <https://doi.org/10.1002/aenm.202002215>.
- [37] P. Wang, Y. Luo, G. Zhang, M. Wu, Z. Chen, S. Sun, Z. Shi, MnO_x-decorated nickel-iron phosphides nanosheets: interface modifications for robust overall water splitting at ultra-high current densities, *Small* 18 (2022) 2105803, <https://doi.org/10.1002/smll.202105803>.
- [38] M. Pan, G. Qian, T. Yu, J. Chen, L. Luo, Y. Zou, S. Yin, Ni modified Co₂VO₄ heterojunction with poor/rich-electron structure for overall urea-rich wastewater oxidation, *Chem. Eng. J.* 435 (2022), 134986, <https://doi.org/10.1016/j.cej.2022.134986>.
- [39] Y. Cao, S. Guo, C. Yu, J. Zhang, X. Pan, G. Li, Ionic liquid-assisted one-step preparation of ultrafine amorphous metallic hydroxide nanoparticles for the highly efficient oxygen evolution reaction, *J. Mater. Chem. A* 8 (2020) 15767–15773, <https://doi.org/10.1039/DOTA00434K>.
- [40] J. Zhao, Y. Zhang, H. Guo, H. Zhang, J. Ren, R. Song, Rational regulation of crystalline/amorphous microprisms-nanochannels based on molecular sieve (VSB-5) for electrochemical overall water splitting, *Small* 18 (2022), e2200832, <https://doi.org/10.1002/smll.202200832>.
- [41] Y. Ren, J. Wang, W. Hu, H. Wen, Y. Qiu, P. Tang, M. Chen, P. Wang, Hierarchical nanostructured Co-Mo-B/CoMoO_{4-x} amorphous composite for the alkaline hydrogen evolution reaction, *ACS Appl. Mater. Interfaces* 13 (2021) 42605–42612, <https://doi.org/10.1021/acsami.1c08350>.
- [42] H. Huang, A. Cho, S. Kim, H. Jun, A. Lee, J.W. Han, J. Lee, Structural design of amorphous CoMoPx with abundant active sites and synergistic catalysis effect for effective water splitting, *Adv. Funct. Mater.* 30 (2020) 2003889, <https://doi.org/10.1002/adfm.202003889>.
- [43] D. Wu, D. Chen, J. Zhu, S. Mu, Ultralow Ru incorporated amorphous cobalt-based oxides for high-current-density overall water splitting in alkaline and seawater media, *Small* 17 (2021), e2102777, <https://doi.org/10.1002/smll.202102777>.
- [44] G. Shi, T. Tano, D.A. Tryk, M. Yamaguchi, A. Iiyama, M. Uchida, K. Iida, C. Arata, S. Watanabe, K. Kakinuma, Temperature dependence of oxygen evolution reaction activity in alkaline solution at Ni-Co oxide catalysts with amorphous/crystalline surfaces, *ACS Catal.* 12 (2022) 14209–14219, <https://doi.org/10.1021/acscatal.2c02586>.
- [45] B. Zhang, J. Shan, X. Wang, Y. Hu, Y. Li, Ru/Rh cation doping and oxygen-vacancy engineering of FeOOH nanoarrays@Ti₃C₂T_x MXene heterojunction for highly efficient and stable electrocatalytic oxygen evolution, *Small* 18 (2022) 2200173, <https://doi.org/10.1002/smll.202200173>.
- [46] H. Zhu, Z. Zhu, J. Hao, S. Sun, S. Lu, C. Wang, P. Ma, W. Dong, M. Du, High-entropy alloy stabilized active Ir for highly efficient acidic oxygen evolution, *Chem. Eng. J.* 431 (2022), 133251, <https://doi.org/10.1016/j.cej.2021.133251>.
- [47] K. Wang, Y. Li, J. Hu, Z. Lu, J. Xie, A. Hao, Y. Cao, Deep reconstruction of transition metal molybdate@hydroxide heterostructure triggered by anion-exchange reaction as high efficiency water oxidation electrocatalyst, *Chem. Eng. J.* 447 (2022), 137540, <https://doi.org/10.1016/j.cej.2022.137540>.
- [48] K. Fan, H. Zou, Y. Ding, N. Dharanipragada, L. Fan, A.K. Inge, L. Duan, B. Zhang, L. Sun, Sacrificial W facilitates self-reconstruction with abundant active sites for water oxidation, *Small* 18 (2022), e2107249, <https://doi.org/10.1002/smll.202107249>.
- [49] S. Liu, S. Geng, L. Li, Y. Zhang, G. Ren, B. Huang, Z. Hu, J.F. Lee, Y.H. Lai, Y. H. Chu, Y. Xu, Q. Shao, X. Huang, A top-down strategy for amorphization of hydroxyl compounds for electrocatalytic oxygen evolution, *Nat. Commun.* 13 (2022) 1187, <https://doi.org/10.1038/s41467-022-28888-3>.
- [50] T.I. Singh, G. Rajeshkhanan, U.N. Pan, T. Kshetri, H. Lin, N.H. Kim, J.H. Lee, Alkaline water splitting enhancement by MOF-derived Fe-Co-Oxide/Co@NC-mNS heterostructure: boosting OER and HER through defect engineering and in situ oxidation, *Small* 17 (2021), e2101312, <https://doi.org/10.1002/smll.202101312>.
- [51] M. Yang, M. Zhao, J. Yuan, J. Luo, J. Zhang, Z. Lu, D. Chen, X. Fu, L. Wang, C. Liu, Oxygen vacancies and interface engineering on amorphous/crystalline CrO(x)-Ni(3)N heterostructures toward high-durability and kinetically accelerated water splitting, *Small* 18 (2022), e2106554, <https://doi.org/10.1002/smll.202106554>.
- [52] S. Shen, Z. Wang, Z. Lin, K. Song, Q. Zhang, F. Meng, L. Gu, W. Zhong, Crystalline-amorphous interfaces coupling of CoSe₂/CoP with optimized d-band center and boosted electrocatalytic hydrogen evolution, *Adv. Mater.* 34 (2022), e2110631, <https://doi.org/10.1002/adma.202110631>.
- [53] S. Sun, X. Zhou, B. Cong, W. Hong, G. Chen, Tailoring the d-band centers endows (Ni_xFe_{1-x})₂P nanosheets with efficient oxygen evolution catalysis, *ACS Catal.* 10 (2020) 9086–9097, <https://doi.org/10.1021/acscatal.0c01273>.
- [54] Y. Lu, K. Huang, X. Cao, L. Zhang, T. Wang, D. Peng, B. Zhang, Z. Liu, J. Wu, Y. Zhang, C. Chen, Y. Huang, Atomically dispersed intrinsic hollow sites of M-M₁-M (M₁=Pt, Ir; M=Fe, Co, Ni, Cu, Pt, Ir) on FeCoNiCuPtIr nanocrystals enabling rapid water redox, *Adv. Funct. Mater.* 32 (2022) 2110645, <https://doi.org/10.1002/adfm.202110645>.
- [55] T.I. Singh, A. Maibam, D.C. Cha, S. Yoo, R. Babarao, S.U. Lee, S. Lee, High-alkaline water-splitting activity of mesoporous 3D heterostructures: an amorphous-shell@crystalline-core nano-assembly of Co-Ni-phosphate ultrathin-nanosheets and V-doped cobalt-nitride nanowires, *Adv. Sci.* 9 (2022), e2201311, <https://doi.org/10.1002/advs.202201311>.
- [56] A. Ali, F. Long, P. Shen, Innovative strategies for overall water splitting using nanostructured transition metal electrocatalysts, *Electrochim. Energy Rev.* 5 (2022) 1, <https://doi.org/10.1007/s41918-022-00136-8>.